



How can CMIP5 AGCMs' resolution influence precipitation in mountain areas: the Hengduan Mountains?

Weichen Tao^{1,2} · Gang Huang^{1,3,4,5} · William K. M. Lau² · Danhong Dong¹ · Pengfei Wang^{1,6} · Guanhuan Wen⁷

Received: 9 May 2019 / Accepted: 19 September 2019
© Springer-Verlag GmbH Germany, part of Springer Nature 2019

Abstract

The precipitation over the Hengduan Mountains (HMs) during rainy seasons is investigated based on observations, reanalysis datasets, and 28 atmospheric general circulation models (AGCMs) from Coupled Model Intercomparison Project phase 5 (CMIP5). Most CMIP5 AGCMs generally capture two observed precipitation centers over the southwestern HMs and on the west side of Sichuan basin (WSSB), but their location, range, and magnitude vary with models. As the horizontal resolution increases, the details of simulated precipitation pattern are improved and closer to observation and reanalysis, as well as the increasing magnitude of precipitation over the southwestern HMs. However, the simulated precipitation on the WSSB is overestimated regardless of resolution. Mechanisms involved in resolution affecting precipitation pattern and biases of precipitation on the WSSB are explored. Representation of topography in AGCMs influences orographic effect, which contributes to simulations of both horizontal and vertical moisture flux convergence and further precipitation over the HMs. The biases of WSSB precipitation between reanalysis and AGCMs are attributed to the discrepancy in the vertical distribution of upward motions. The simulated upward motions can reach a higher level than reanalysis, and a spurious center of upward motions develops at 400 hPa due to the overestimation of circulation-precipitation feedback in AGCMs.

Keywords The Hengduan Mountains · Rainy-season precipitation · CMIP5 · Model resolution · Topography · Orographic effect · Circulation-precipitation feedback

1 Introduction

The Hengduan Mountains (HMs) lie on the southeast side of the Tibetan Plateau (TP) and west side of Sichuan basin (WSSB), with the YunGui plateau and Bayan Har Mountains on south and north sides, respectively (Li et al. 2011; Zhang

et al. 2014; Fang et al. 2017; Dai et al. 2018; Dong et al. 2018, 2019). The HMs feature the world's steepest elevation drop from about 4800 m to 600 m from the TP to Sichuan basin within a distance of 500 km and divide the first and second steps of China's topography (Fig. 1). Mountains and rivers alternate there as the unique 3-dimensional landscape featured with high mountains and deep valleys, flourishing in a diverse ecosystem consisting of rivers, lakes, forests, grasslands, and glaciers. Several major rivers in China and

Electronic supplementary material The online version of this article (<https://doi.org/10.1007/s00382-019-04993-w>) contains supplementary material, which is available to authorized users.

✉ Gang Huang
hg@mail.iap.ac.cn

- ¹ State Key Laboratory of Numerical Modeling for Atmospheric Sciences and Geophysical Fluid Dynamics, Institute of Atmospheric Physics, Chinese Academy of Sciences, Beijing 100029, China
- ² Earth System Science Interdisciplinary Center, University of Maryland, College Park, MD 20740, USA
- ³ Laboratory for Regional Oceanography and Numerical Modeling, Qingdao National Laboratory for Marine Science and Technology, Qingdao 266237, China

- ⁴ Joint Center for Global Change Studies, Beijing 100875, China
- ⁵ University of Chinese Academy of Sciences, Beijing 100049, China
- ⁶ Center for Monsoon System Research, Institute of Atmospheric Physics, Chinese Academy of Sciences, Beijing 100029, China
- ⁷ Guangzhou Institute of Tropical and Marine Meteorology, China Meteorological Administration, Guangzhou 510080, China

Indochina Peninsula originate from or flow through this region. Moreover, precipitation over HMs is crucial to the formation of glaciers, the supply of fresh water from surface runoffs, and river discharge (Dong et al. 2016), thus it has a great impact on the hydrological cycle, ecological environment, and social economy in both local and remote downstream areas.

The HMs possess a typical monsoon climate with distinct rainy and drought seasons. The rainy seasons start from May to September, when the total precipitation accounts for more than 80% of annual total precipitation (Dong et al. 2018, 2019). During rainy seasons, the HMs are the transition zone between the South Asian and East Asian monsoons, and prevail southwest winds at lower-level, transporting moisture from the ocean (Fig. 1). The winds blow roughly parallel to the elevation gradient on the southwest side of HMs, and the orographic effects could be clearly observed in the spatial distribution of climatological rainy-season precipitation, as precipitation to increase with elevation along the windward slopes of HMs (Fig. 1). The topography modifies the precipitation distribution through orographically forced mechanical lifting. Incoming moisture transported by the monsoon southwesterlies is forced to rise parallel to the slope, resulting in condensation and precipitation on the windward side (Smith 1979; Barros and Lettenmaier 1993, 1994; Roe 2005; Lau and Kim 2006; Hughes et al. 2009; Hu et al. 2017). Besides, topography also can alter atmospheric circulation

due to its barrier effect, and lower-level convergence associated with upward motions are generated, contributing to the precipitation on the windward slopes (Katzfey 1995; Jiang 2003; Roe 2005; Cannon et al. 2017; Mishra et al. 2018).

Mountain areas are often remote and have a coarse monitoring network, and numerical models are useful tools for estimating orographic precipitation in these regions (e.g., Chen and Huang 1999; Ferretti et al. 2000; López-Moreno et al. 2008). Besides, climate models have been widely used to study monsoon-related circulation and precipitation (e.g., Goswami 1998; Kang et al. 2002; Zhou and Li 2002; Lau et al. 2006; Ueda et al. 2009; Song et al. 2012; Sperber et al. 2013; Ashfaq et al. 2017; Tao et al. 2018), and HMs belong to the monsoon region accompanied by complex topography. Therefore, it is necessary to develop the higher horizontal resolution models, which are capable of simulating regional climate with a high degree of fidelity. The horizontal resolution significantly contributes to the biases of models simulating spatial distribution, frequency, magnitude, and seasonal cycle of precipitation over the mountain or monsoon areas in two key ways: inadequate performance of physical and dynamical processes (Kang et al. 2002; Zhou and Li 2002; Kripalani et al. 2007; Duan et al. 2013; Huang et al. 2013; Hunt and Turner 2017; Shang et al. 2019) and inaccurate representation of complex topography (Sperber et al. 1994; Sperber et al. 2013; Cannon et al. 2017; Ogata et al. 2017; Mishra et al. 2018). The accuracy of topography in

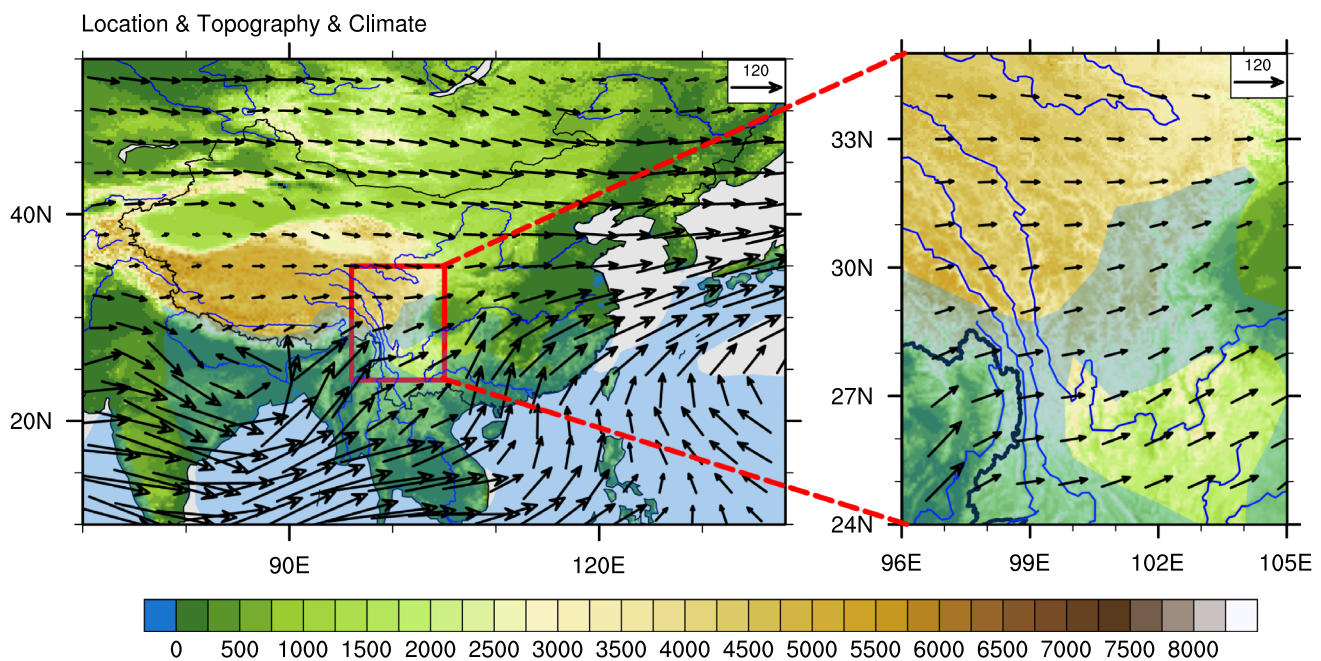


Fig. 1 Geographic location, topography (shaded; m) from ETOPO1, and climatology of rainy-season column-integrated moisture flux (vector; $\text{kg s}^{-1} \text{m}^{-1}$) and precipitation (blue shading, mm) from reanalysis of the HMs. HMs region (24° – 35°N , 96° – 105°E) is marked

by a red box. Topography is shaded as the green and brown label bar at the bottom, and the blue shading denotes precipitation greater than 6 mm

models also influences the generation and propagation of orographically triggered atmospheric waves, which affect the remote regions outside the mountain domain (Chen and Bordoni 2014; Yao et al. 2017). Generally, even with no change in physical representation, high-resolution models (HRMs) improve to various degree, the simulations of multi-scale interactions, involving regional climate, circulation, atmospheric teleconnections, air-sea coupling, and so on (e.g., Sperber et al. 1994; Maloney and Chelton 2006; Kitoh and Kusunoki 2008; Hertwig et al. 2015; Prodhomme et al. 2016; Ogata et al. 2017).

The aim of present paper is to evaluate the ability of 28 atmospheric general circulation models (AGCMs) from the World Climate Research Programme's Coupled Model Intercomparison Project phase 5 (CMIP5) for Fifth Assessment Report (Taylor et al. 2011) in simulating rainy-season precipitation over the HMs. We show clear evidence that the simulations of HMs precipitation patterns are significantly influenced by the resolution of AGCMs, and HRMs can better reproduce the observed spatial features of HMs precipitation than the rest lower-resolution models, as well as the stronger magnitude of precipitation over the southwestern HMs. In addition, consistent overestimation of precipitation on the WSSB appears in most AGCMs regardless of model resolution, and this bias originates from the excessively strong interaction between circulation and precipitation according to the results of the dynamical analysis. The rest of the paper is organized as follows. Section 2 describes the data and CMIP5 AGCMs. The main results are presented in Sect. 3, followed by a concluding summary in Sect. 4.

2 Data and models

The observed precipitation data used in this study is from the National Meteorological Information Center of the China Meteorological Administration (NMIC/CMA). It is available since 1961 with a spatial resolution of $0.5^\circ \times 0.5^\circ$ and generated from over 2400 rain gauges of China by using thin plate spline interpolation, with Global 30 Arc-Second Elevation (GTOPO30) model incorporated to eliminate the influence of elevation. This is a high-quality dataset widely used in previous studies (e.g., Xu et al. 2009; You et al. 2015; Wang et al. 2018). The observed topography dataset is from Earth topography one arc-minute grid (ETOPO1; Amante and Eakins 2009) that is a 1 arc-minute global relief model of Earth's surface that integrates land topography and ocean bathymetry derived from several sources on a $1' \times 1'$ grid and is available at <https://www.ngdc.noaa.gov/mgg/global/global1.html>. Monthly atmospheric variables used in this study are obtained from European Centre for Medium-Range Weather Forecasts (ECMWF) interim reanalysis (ERA-Interim; Dee et al. 2011) with approximately $0.7^\circ \times 0.7^\circ$ spatial resolution

at 37 pressure levels. The variables include horizontal winds, vertical velocity, specific humidity, air temperature, precipitation, evaporation, surface pressure, and surface geopotential height. The Japanese 55-year Reanalysis (JRA-55) on a $1.25^\circ \times 1.25^\circ$ horizontal resolution at 37 pressure levels, compiled by the Japan Meteorological Agency (Kobayashi et al. 2015; Harada et al. 2016) is also used, and both ERA-Interim and JRA-55 exhibit the consistent results. Hereinafter "reanalysis" represents their ensemble mean results except otherwise specified.

The present study is based on the Atmospheric Model Intercomparison Project (AMIP) experiments of 28 CMIP5 AGCMs, which were forced by observed sea surface temperature and sea ice for the period from 1979 to 2008. Monthly mean outputs are used, and the including variables are the same as the reanalysis datasets. Only one member (r1i1p1) of each model simulations is analyzed. The detailed information about names and resolutions of 28 CMIP5 AGCMs is listed in Table 1. All AMIP outputs, observations, and reanalysis datasets are remapped onto a uniform $1^\circ \times 1^\circ$ grid by using bilinear interpolation except otherwise specified, and the period of above data is selected from 1979 to 2008 to match the length of AMIP experiments. Note that, for the models with low resolution, remapping onto a high-resolution grid does not alter the major conclusions.

3 Result

3.1 Evaluation of HMs precipitation with model resolution and biases

Figure 2 shows the climatological precipitation over HMs during rainy seasons in observation, reanalysis, and 28 CMIP5 AGCMs. The spatial distribution of precipitation in observation is not geographically homogeneous but varies from south to north, and precipitation is mainly concentrated along the windward slopes, indicating the precipitation-topography relationship. The maximum precipitation center is observed on the WSSB, and default values appear over the southwestern HMs due to the limitation of observed data, which does not include rain gauges outside of China. The reanalysis results show maximum precipitation center locating over the southwestern HMs, and the precipitation center on the WSSB is reasonably reproduced. Another observed monthly precipitation with $0.25^\circ \times 0.25^\circ$ spatial resolution from the Tropical Rainfall Measuring Mission (TRMM) 3B43 dataset provided by National Aeronautics and Space Administration (Huffman et al. 2007) is used to confirm the results of gauge-based observation and reanalysis during their overlapping period from 1998 to 2008. The HMs precipitation patterns are highly resembling among these datasets (Fig. S1 in the supplemental material). Thus, CMIP5

Table 1 The names and resolutions of 28 CMIP5 AGCMs used in this study

Number	Model	Resolution (lon × lat)
1	ACCESS1-0	1.875 × 1.25
2	ACCESS1-3	1.875 × 1.25
3	bcc-csm1-1	2.8 × 2.8
4	bcc-csm1-1-m	1.1 × 1.1
5	BNU-ESM	2.8 × 2.8
6	CanAM4	2.8 × 2.8
7	CCSM4	1.25 × 1
8	CMCC-CM	0.75 × 0.75
9	CNRM-CM5	1.4 × 1.4
10	CSIRO-Mk3-6-0	1.875 × 1.875
11	FGOALS-g2	2.8 × 3
12	GFDL-CM3	2.5 × 2
13	GFDL-HIRAM-C180	0.6 × 0.5
14	GFDL-HIRAM-C360	0.3 × 0.25
15	GISS-E2-R	2.5 × 2
16	HadGEM2-A	1.875 × 1.25
17	inmcm4	2 × 1.5
18	IPSL-CM5A-LR	3.75 × 1.875
19	IPSL-CM5A-MR	2.5 × 1.25
20	IPSL-CM5B-LR	3.75 × 1.875
21	MIROC5	1.4 × 1.4
22	MIROC-ESM	2.8 × 2.8
23	MPI-ESM-LR	1.875 × 1.875
24	MPI-ESM-MR	1.875 × 1.875
25	MRI-AGCM3-2H	0.55 × 0.55
26	MRI-AGCM3-2S	0.18 × 0.18
27	MRI-CGCM3	1.125 × 1.125
28	NorESM1-M	2.8 × 1.875

The high-resolution models are shown in bold font

AGCMs are compared with reanalysis, which is close to gauge-based observation gauge-based observation but exhibits a more complete HMs precipitation pattern.

Most CMIP5 AGCMs generally capture the two precipitation centers in reanalysis, but their location, range, and magnitude vary with models. The spatial distribution of HMs precipitation simulated by HRMs is closer to reanalysis than the other models, although the precipitation center on the WSSB is much stronger in HRMs. Further analysis measures the degree of fidelity in simulating HMs precipitation pattern compared with reanalysis by using pattern correlation and area root-mean-square-difference (RMSE), and their connections to model resolution are shown in Fig. 3. HRMs exhibit higher pattern correlation and lower area RMSE than relative lower-resolution models. The pattern correlation and area RMSE are correlated with model resolution at -0.61 and 0.48 , reaching 99% and 95% significant level, respectively. The pattern correlation-resolution and area RMSE-resolution relationship are

confirmed by using 84 members from the 28 CMIP5 AGCMs (Fig. S2), further emphasizing the dominant role of model resolution in the inter-model diversity of HMs precipitation. The detailed member information of each model is given in Table S1. Note that some AGCMs (e.g., ACCESS1-0, GISS-E2-R, and HadGEM2-A) appear to be outliers, indicating that other factors, like the biases in simulations of monsoon, circulation response to the topography, circulation-precipitation feedback, and so on, which may originate from the biases of physical scheme and dynamical frame, cause the weaknesses in representation of precipitation processes in these models and obscure the HMs precipitation-resolution relationship.

Next, the 28 CMIP5 AGCMs are divided into 3 groups: low-resolution models (LRMs), medium-resolution models (MRMs), and HRMs, which are defined as horizontal resolution greater than 2 degrees, greater than 1 degree and less than 2 degrees, and less than 1 degree, respectively. Figure 4c–e present the ensemble mean of HMs precipitation in 3 groups of CMIP5 AGCMs, respectively. Indeed, as the horizontal resolution increases, the simulated precipitation pattern is improved and closer to observation and reanalysis (Figs. 3, 4), as well as the increasing magnitude of precipitation over the southwestern HMs (Fig. 4b–e). However, the simulated precipitation on the WSSB is overestimated regardless of resolution (Fig. 4a–e), and consistent results are also obtained in each individual model (Fig. 2), probably due to the systematic biases in representation of moist convective processes in all AGCMs. The similar spatial features of HMs precipitation in the three groups divided by resolution are obtained by using a larger ensemble of 84 members from 28 CMIP5 AGCMs (Fig. S3). To examine the physical processes involved in resolution affecting precipitation pattern and biases of precipitation on the WSSB, the solution to moisture budget analysis is performed in the next subsection.

3.2 Moisture budget analysis

Assuming steady state equilibrium in long-term mean, the climatological rainy-season precipitation over HMs can be diagnosed as

$$\bar{P} = -\overline{\langle \nabla \cdot (\mathbf{V}q) \rangle} - \overline{\langle \partial_p \omega q \rangle} + \bar{E},$$

where overbars denote climatology state, P is precipitation, $\mathbf{V} = (u, v)$ is the horizontal wind velocity, q is specific humidity, ω is vertical velocity, E is evaporation, and the angle brackets denotes a mass integration from the surface to 100 hPa. In present study, the vertical term $\left(-\overline{\langle \partial_p \omega q \rangle}\right)$ can not be neglected due to the significant surface vertical velocity forced by complex topography of HMs.

The results of moisture budget analysis based on reanalysis, LRMs, MRMs, and HRMs are presented in Fig. 5. The diagnosed results show the dominant contribution of vertical

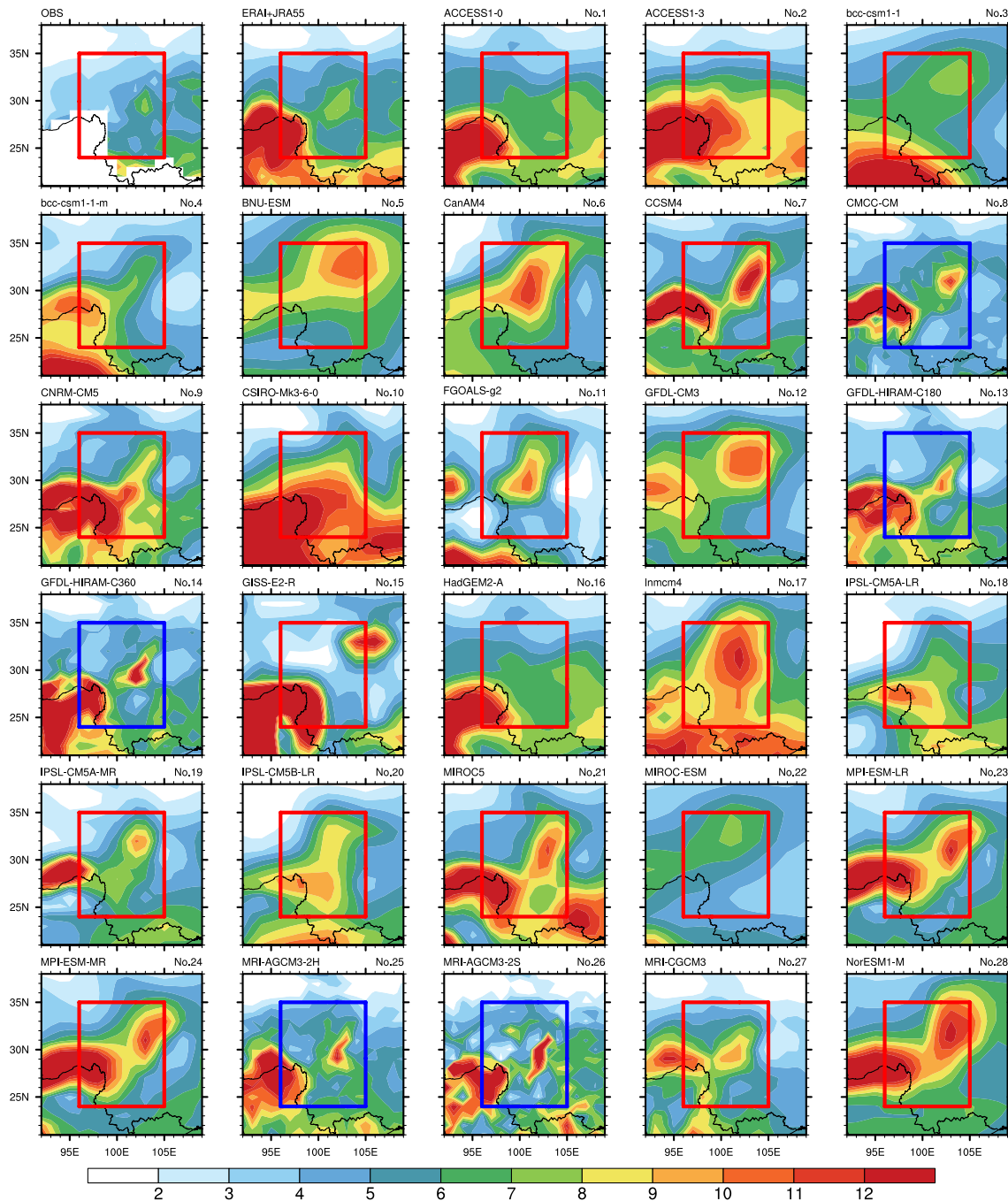


Fig. 2 Climatological precipitation (mm) over HMs during rainy seasons in observation, reanalysis, and 28 CMIP5 AGCMs. Blue boxes denote the HMs regions in the top 5 high-resolution models. Model

names and numbers are given on the top left and right of panels, respectively, and “OBS” and “ERA1+JRA55” represent observation and reanalysis, respectively

moisture flux convergence term $(-\overline{\partial_p \omega q})$ to climatological rainy-season precipitation over HMs in both reanalysis and AGCMs, compared with the other terms. Being similar to precipitation, the simulated vertical moisture flux convergence is closer to reanalysis with the increase of model resolution, and observed details of vertical moisture flux

convergence pattern are precisely captured in HRMs, especially on the WSSB and over the southwestern HMs (Fig. 5a–d, i–l). Note that the magnitude of simulated vertical moisture flux convergence on the WSSB is not greater than reanalysis, even though there is stronger precipitation in AGCMs. The cross-section of vertical moisture flux convergence $(-\partial_p \omega q)$, vertical velocity (ω) , and specific

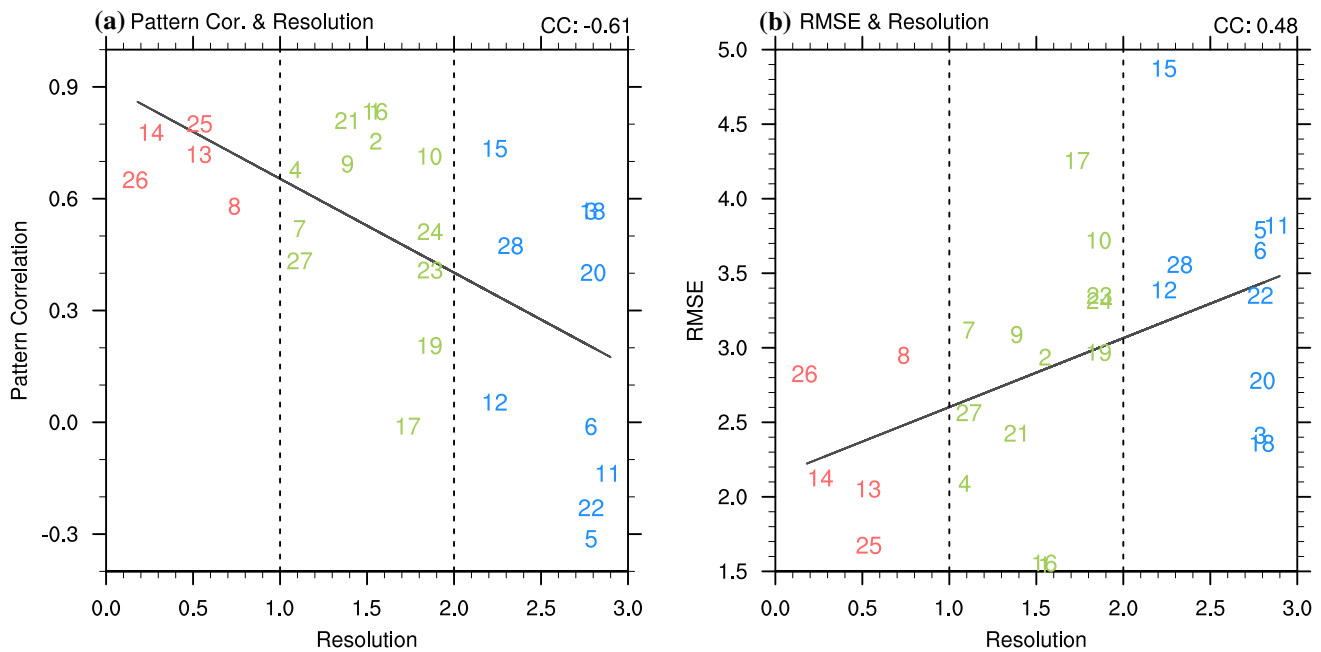


Fig. 3 Scatter diagram of model resolution (abscissa) and **a** pattern correlation between CMIP5 AGCMs and reanalysis (ordinate), and **b** area root-mean-square-difference between CMIP5 AGCMs and reanalysis (ordinate). Numbers represent the model numbers listed in Table 1. Model resolution is calculated by averaging zonal and merid-

ional resolutions. Blue, green, and red numbers denote the LRM, MRM, and HRM defined as model resolution greater than 2 degrees, greater than 1 degree and less than 2 degrees, and less than 1 degree, respectively. The lines are the best fit lines for the scatters. The correlation coefficients are given on the top right corner of each panel

humidity (q) in these two areas are examined in Figs. 6 and 7. The vertical distribution of vertical moisture flux convergence in reanalysis and AGCMs are highly consistent with that of vertical velocity, emphasizing the crucial role of upward motions. The overestimation of precipitation on the WSSB is probably related to vertical distribution of upward motions, and the relevant mechanism will be explored in next two subsections.

On the other hand, the vertical moisture flux convergence term ($-\langle \partial_p \omega q \rangle$) is partially offset by horizontal moisture flux convergence term ($-\langle \nabla \cdot (\mathbf{V}q) \rangle$), especially near the ridges of the Himalayas and HMs (Figs. 1, 5e–h). In reanalysis, there is horizontal moisture flux convergence on windward slopes of the Himalayas, contributing to precipitation in the southwest corner of HMs (Fig. 5a, e). This positive contribution of horizontal moisture flux convergence term ($-\langle \nabla \cdot (\mathbf{V}q) \rangle$) to precipitation is generally captured in HRMs, less so in MRMs, and totally missing in LRMs (Fig. 5f–h). Therefore, as model resolution increases, the precipitation over the southwestern HMs becomes stronger, and its meridional range becomes wider (Fig. 5b–d), owing to the influence of horizontal moisture flux convergence term ($-\langle \nabla \cdot (\mathbf{V}q) \rangle$).

3.3 Orographic effect

Previous results point out that model resolution can influence simulations of both horizontal and vertical moisture flux convergence and further precipitation pattern over the HMs, where precipitation is mainly concentrated along the windward slopes of Himalayas and HMs, indicating the contribution of resolution-related topography. As shown in the cross-section of vertical velocity over the southwestern HMs in reanalysis (Fig. 6a–e), the center of upward motions is close to surface on the windward slopes, evidencing the effect of orographically forced mechanical lifting. Worth noting is that, the upward motions can reach more than 200 hPa near the southern and western boundaries of HMs, where the effects of lower-level convergence are strongest, as the horizontal moisture flux convergence shown in Fig. 5e. The topography over the Himalayas and HMs weakens southwest winds through its barrier effect, and the lower-level convergence is generated, contributing to the horizontal moisture flux convergence and upward motions over the southwestern HMs.

The HRMs simulated upward motions more resemble the reanalysis results than the other two groups of AGCMs, especially near the southern and western boundaries of HMs (Fig. 6a–d, e–h). Moreover, the upward motions due to orographically forced mechanical lifting along the windward slopes in LRMs and MRMs extend farther than HRMs

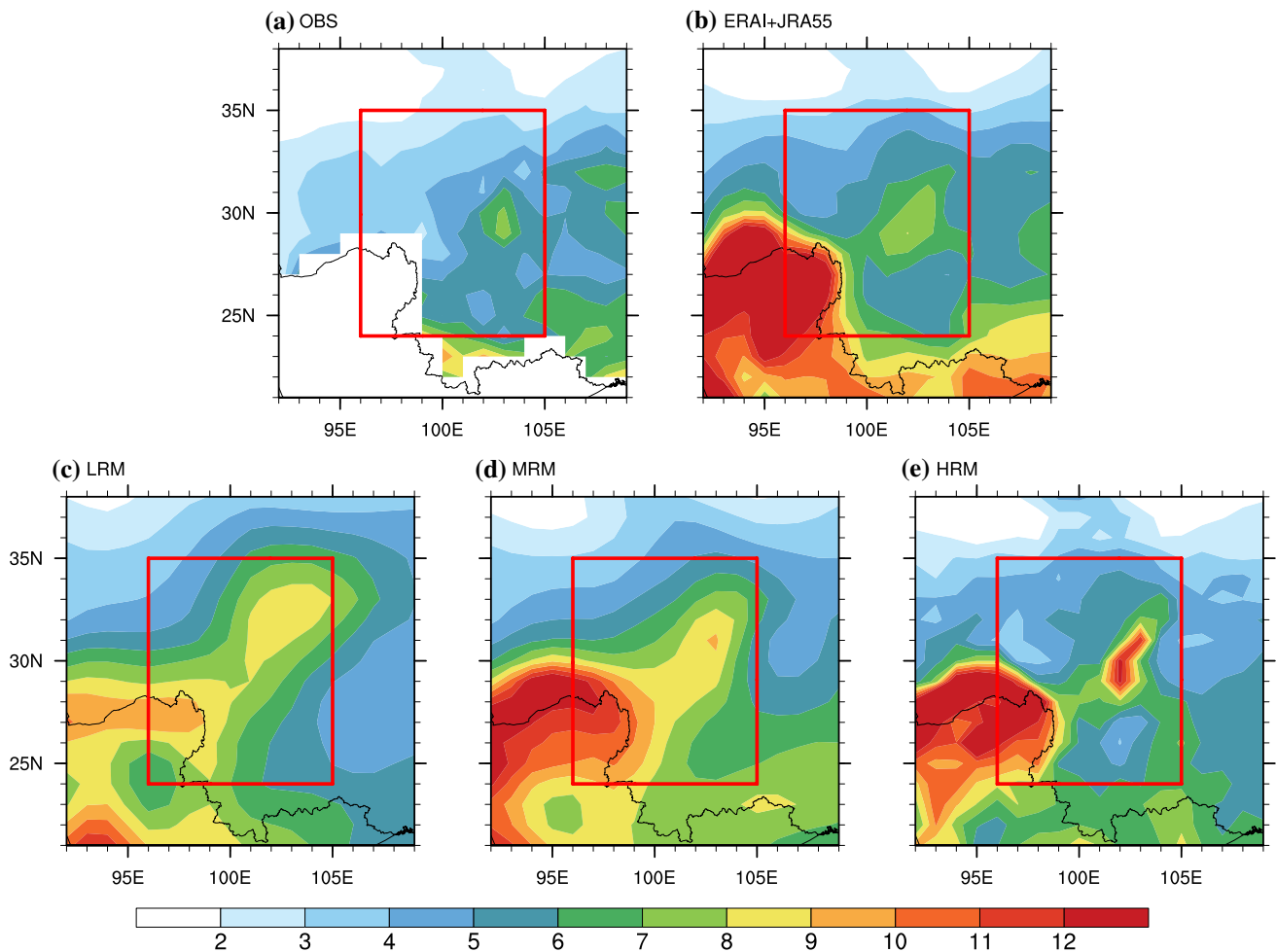


Fig. 4 Climatological precipitation (mm) over HMs during rainy seasons in **a** observation, **b** reanalysis, **c** LRMs, **d** MRMs, and **e** HRMs

(Fig. 6b–d, f–h). Higher-resolution models can better represent the complex topography, which weakens atmospheric circulation by increasing orographic roughness and further enhances the horizontal moisture flux convergence and upward motions (Figs. 5h, 6d–h). On the contrary, smoother topography in lower-resolution models is skewed to intensification of atmospheric circulation with farther extension upwind and fails to simulate horizontal moisture flux convergence and upward motions along the windward slopes of the Himalayas and HMs (Figs. 5f, 6b–f). The stronger cross-barrier moisture transports in LRMs even lead to the northward shift of horizontal moisture flux convergence on the north side of Sichuan basin (Fig. 5f). Note that the horizontal moisture flux convergence on windward slopes of the Himalayas and HMs in HRMs is still weaker than reanalysis, indicating underestimation of orographic barrier effect in AGCMs (Fig. 5e–h; Mishra et al. 2018).

On the other hand, the effect of orographically forced mechanical lifting varies according to the different

resolution-related topography. The orographically forced mechanical lifting can be written as

$$\omega_s = \mathbf{V} \cdot \nabla P_s,$$

ω_s and P_s represent vertical velocity due to orographically forced mechanical lifting, surface pressure, respectively. Figure 8 shows the rainy-season vertical velocity due to orographically forced mechanical lifting over HMs in reanalysis and AGCMs. The topography directly forced ascents develop along the windward slopes of the Himalayas and HMs, and their spatial distribution partially resemble vertical moisture flux convergence and precipitation (Figs. 5a–d, i–l, 8). The results for HRMs are close to those for reanalysis (Fig. 8a–d), and the magnitude and range of topography directly forced ascents become weaker and wider with the decrease of model resolution from MRMs to LRMs, respectively (Fig. 8b, c). Note that Fig. 8 is calculated through interpolating relevant variables onto a $0.5^\circ \times 0.5^\circ$ grid. Surface pressure is closely related to topography height, thus horizontal gradients of surface pressure (∇P_s) are sensitive

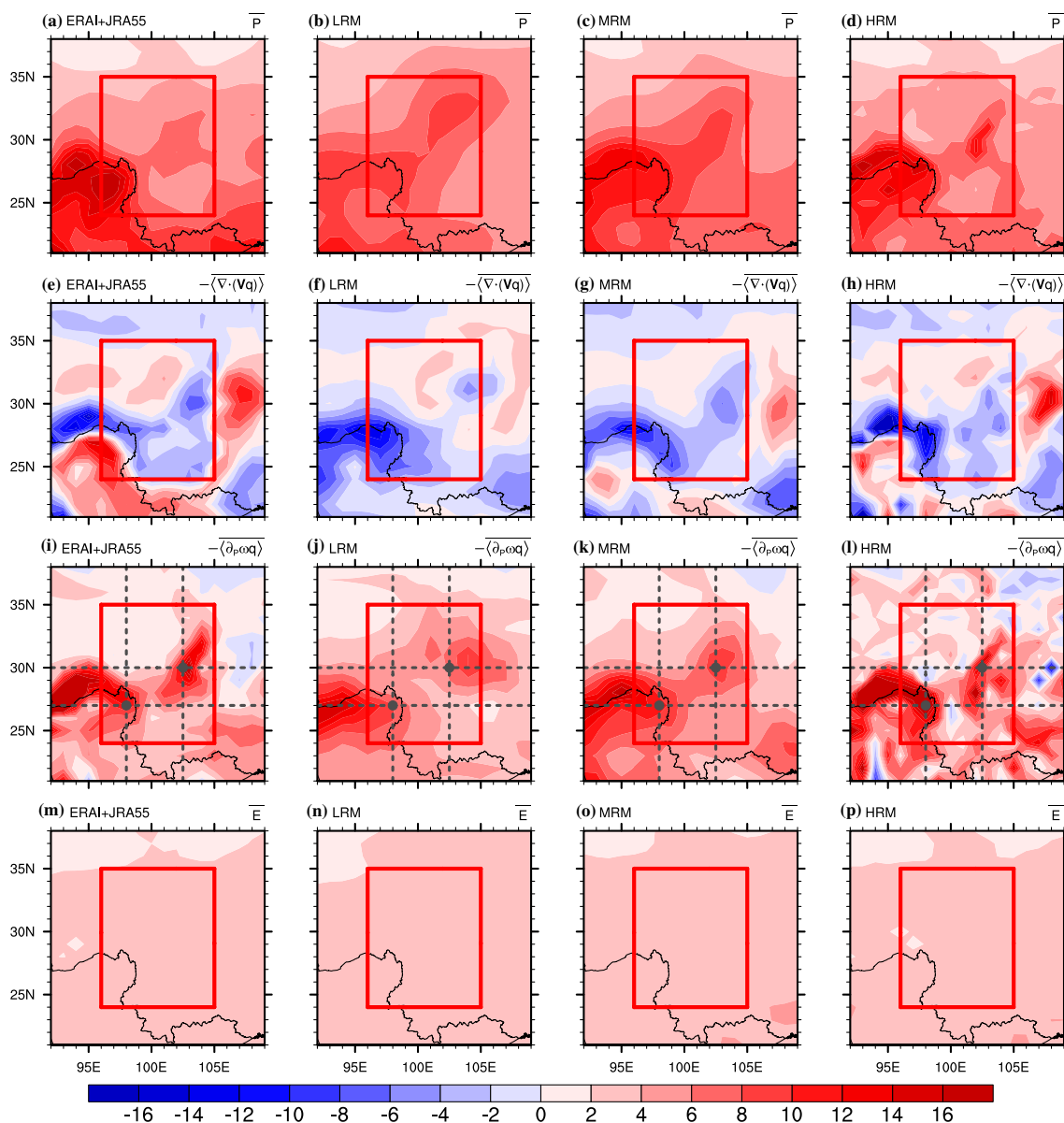


Fig. 5 Diagnosed climatological precipitation over HMs during rainy seasons in **a, e, i, m** reanalysis, **b, f, j, n** LRMs, **c, g, k, o** MRMs, and **d, h, l, p** HRMs. Shown from top to bottom panels are precipitation term (\bar{P} ; mm), vertically integrated horizontal moisture flux convergence term ($-\overline{(\nabla \cdot \mathbf{V}q)}$); mm), vertically integrated vertical moisture

flux convergence term ($-\overline{(\partial_p \omega q)}$; mm), and evaporation term (\bar{E} ; mm). Dots denote the locations of southwestern HMs (27°N , 98°E) and WSSB (30°N , 102.5°E), where the zonal and meridional cross-section along the dashed lines are obtained

to horizontal resolution. Interpolating surface pressure onto a coarse resolution results in a weak bias of gradient term (∇P_s) in ERAI and HRMs, whereas the original resolutions of which are relatively high.

The vertical moisture flux convergence shows the dominant contribution to the precipitation on the WSSB (Fig. 5a–d, i–l) and is related to the vertical distribution of upward motions (Fig. 7). The resolution-related orographic barrier effect and orographically forced mechanical lifting play a similar role in upward motions on the

WSSB, as their weaker magnitude and wider range with the more northeastward shift in LRMs and MRMs than HRMs (Figs. 7b–d, f–h, 8b–d). Besides, the cross-section of simulated upward motions has two centers: one closes to surface and the other is at 400 hPa (Fig. 7b–d, f–h), while only one center near the surface is observed in reanalysis (Fig. 7a, e). The discrepancy in the vertical distribution of upward motions between reanalysis and AGCMs influences WSSB precipitation through vertical moisture flux convergence ($-\partial_p \omega q$), which can be decomposed into

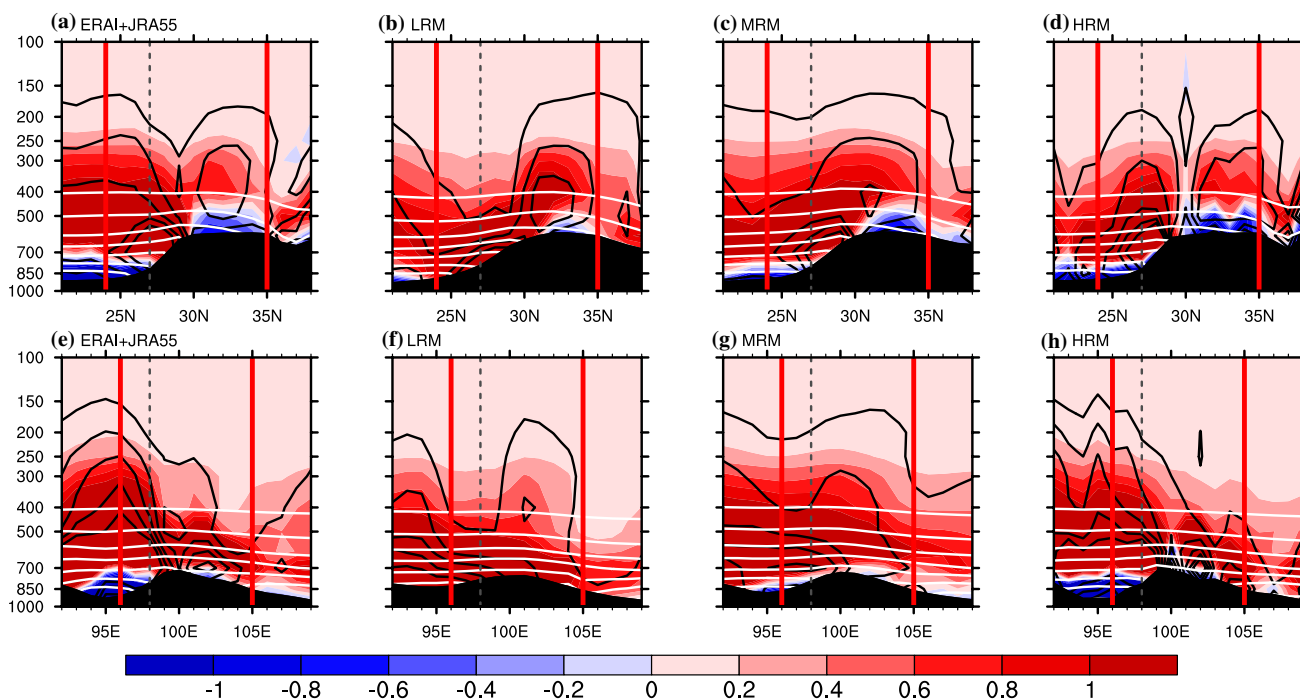


Fig. 6 Zonal cross-section of vertical moisture flux convergence term ($-\partial_p \omega q$; shaded; mm), vertical velocity (ω ; black contour; CI is 0.02 Pa s^{-1}), and specific humidity (q ; white contour; CI is 0.002 g g^{-1}) for the southwestern HMs in **a** reanalysis, **b** LRMs, **c**

MRMs, and **d** HRMs. **e-h** are as in **a-d**, but for meridional cross-section. Red lines denote the boundaries of HMs, and grey dashed lines denote the location of southwestern HMs

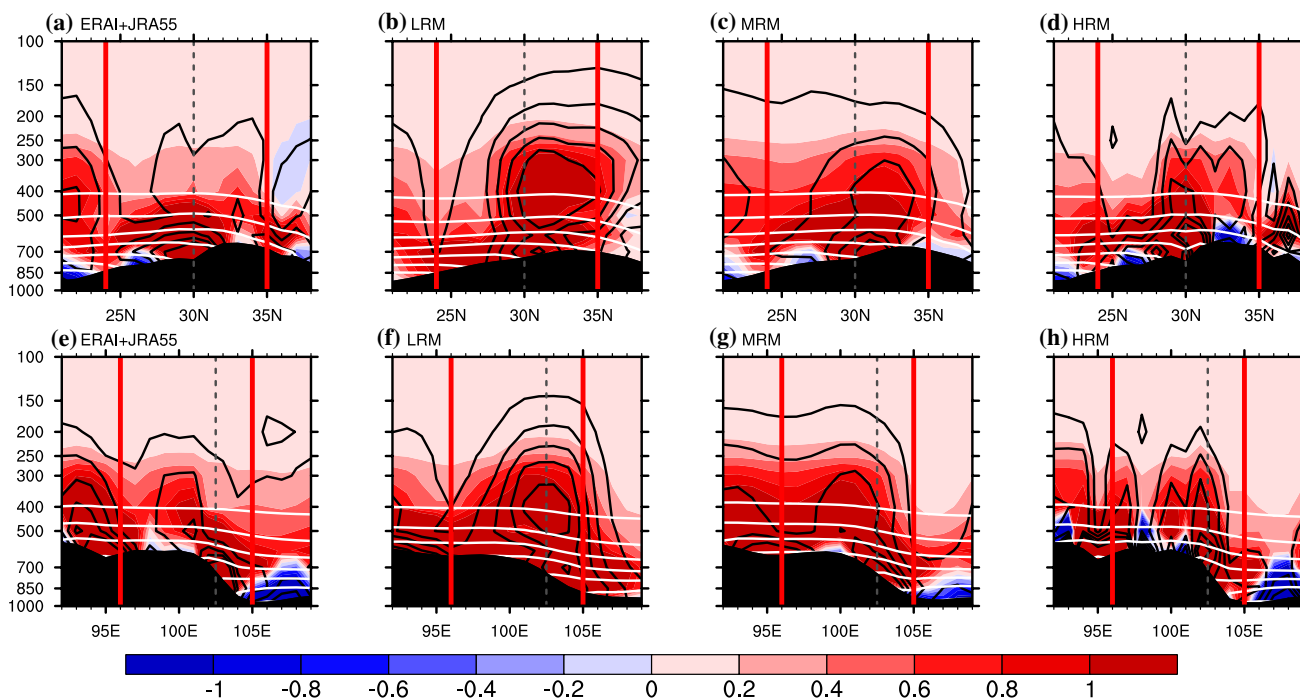


Fig. 7 As Fig. 6, but for the WSSB

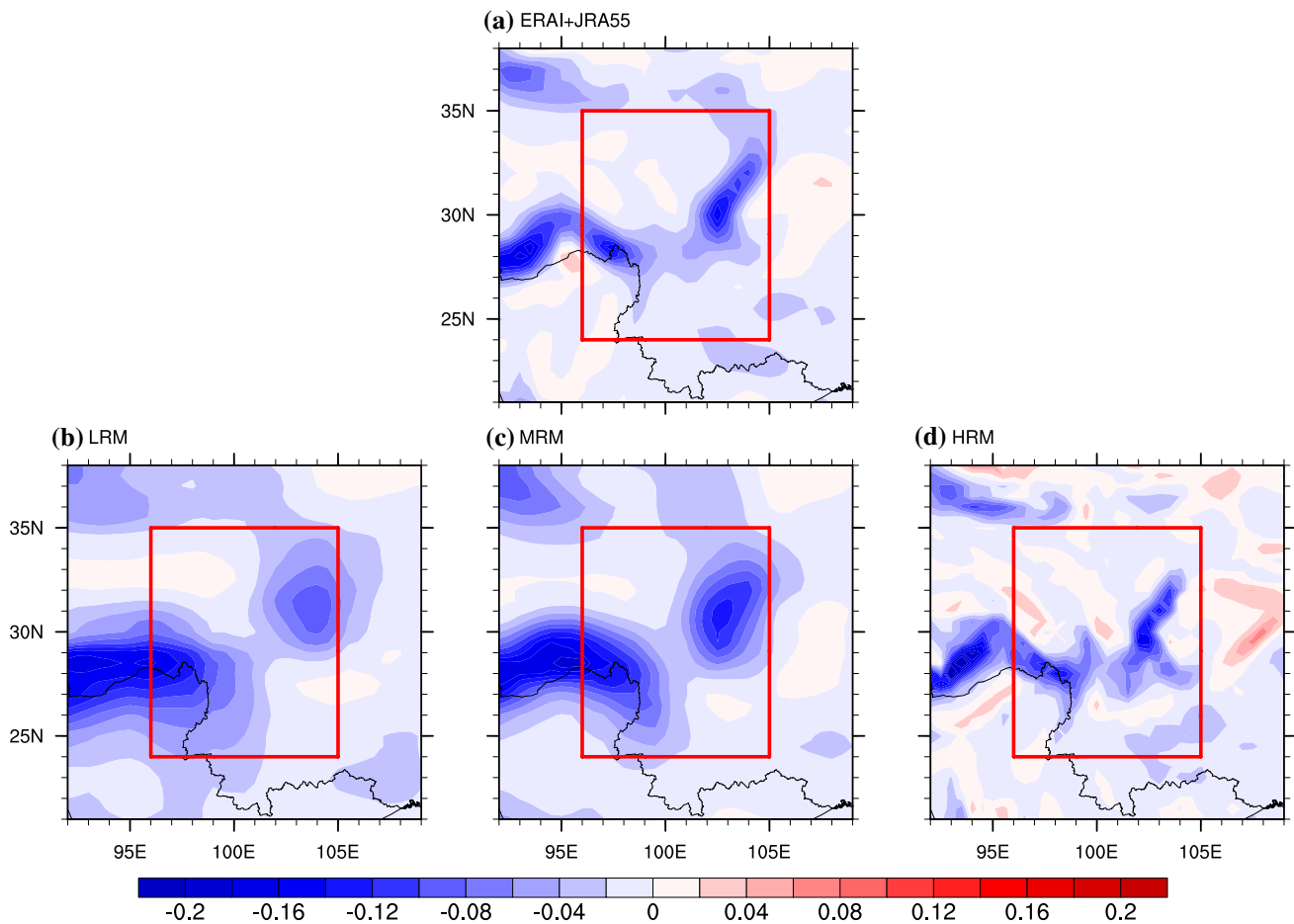


Fig. 8 Climatological vertical velocity (Pa s^{-1}) due to orographically forced mechanical lifting over HMs during rainy seasons in **a** reanalysis, **b** LRMs, **c** MRMs, and **d** HRMs

vertical moisture advection ($-\omega\partial_p q$) and vertical velocity convergence ($-q\partial_p\omega$). Reanalysis results show that the vertical velocity convergence ($-q\partial_p\omega$) is dominant in vertical moisture flux convergence ($-\partial_p\omega q$), while a stronger contribution of vertical moisture advection ($-\omega\partial_p q$) is obtained from AGCMs (Fig. S4). The topography exerts a stronger effect on upward motions in reanalysis and HRMs than MRMs and LRMs, as shown in the magnitude of near surface ascent center for vertical distribution and topography directly forced ascents on the WSSB for spatial distribution (Figs. 7, 8). Thus, beside the orographic effect, there must be an additional mechanism involved in the 400 hPa ascent center contributes to the overestimation of precipitation on the WSSB in AGCMs.

3.4 Omega equation analysis

The omega equation is used to diagnose rainy-season vertical velocity at 400 hPa, where shows the maximum

values in the cross-section of upward motions on the WSSB (Fig. 7b–d, f–h):

$$\omega = \left(\sigma \nabla^2 + f^2 \frac{\partial^2}{\partial P^2} \right)^{-1} f \frac{\partial}{\partial P} [\mathbf{V} \cdot \nabla (\zeta + f)] + \left(\sigma \nabla^2 + f^2 \frac{\partial^2}{\partial P^2} \right)^{-1} \times \frac{R}{P} \nabla^2 (\mathbf{V} \cdot \nabla T) - \left(\sigma \nabla^2 + f^2 \frac{\partial^2}{\partial P^2} \right)^{-1} \frac{R}{c_p P} \nabla^2 \frac{dQ}{dt},$$

where $\sigma = (R/P) \left(\frac{RT}{c_p P} - \frac{dT}{dP} \right)$ is static stability, f is Coriolis parameter, P is air pressure, ζ is relative vorticity, R is gas constant, T is air temperature, c_p is specific heat at constant pressure, Q is diabatic heating. The terms on the right side of equation denote the vertical velocity due to the vertical difference of horizontal vorticity advection (ω_{vor}), vertical velocity due to horizontal temperature advection (ω_{temp}), and vertical velocity due to diabatic heating (ω_Q), respectively. Note that daily data is needed for the calculation of diabatic heating (Q), and is incomplete in many CMIP5 AGCMs. Thus, $\omega_Q = \omega - \omega_{vor} - \omega_{temp}$ is calculated as a substitute.

Figure 9 shows diagnosed results for omega equation in reanalysis and AGCMs. There are downward motions caused by the combined effect of the vertical difference of horizontal vorticity advection and horizontal temperature advection on the WSSB (Fig. 9e–h), where appears diabatic heating forced upward motions (Fig. 9i–l). Diabatic heating in monsoon area is mainly contributed by precipitation released latent heat, and there is a close relationship between precipitation and circulation (Jin et al. 2013; Li et al. 2017; Tao et al. 2017; Dong et al. 2019). Thus, the vertical velocity due to diabatic heating (ω_Q) can be considered as a feedback between circulation and precipitation (Hu et al. 2017). The WSSB upward motions induced by diabatic heating in AGCMs are significantly stronger than reanalysis, indicating that the circulation-precipitation feedback is overestimated in AGCMs. As a result, the biases of WSSB precipitation between reanalysis and AGCMs

are attributed to the discrepancy in the vertical distribution of upward motions. The simulated upward motions can reach a higher level than reanalysis, and a spurious center of upward motions develops at 400 hPa due to the overestimation of circulation-precipitation feedback in AGCMs.

4 Summary

The precipitation over the HMs during rainy seasons is investigated based on observations, reanalysis datasets, and 28 CMIP5 AGCMs. The observation and reanalysis results show that precipitation is mainly concentrated along the windward slopes, and two significant precipitation centers are observed over the southwestern HMs and on the WSSB. Most CMIP5 AGCMs generally capture two precipitation

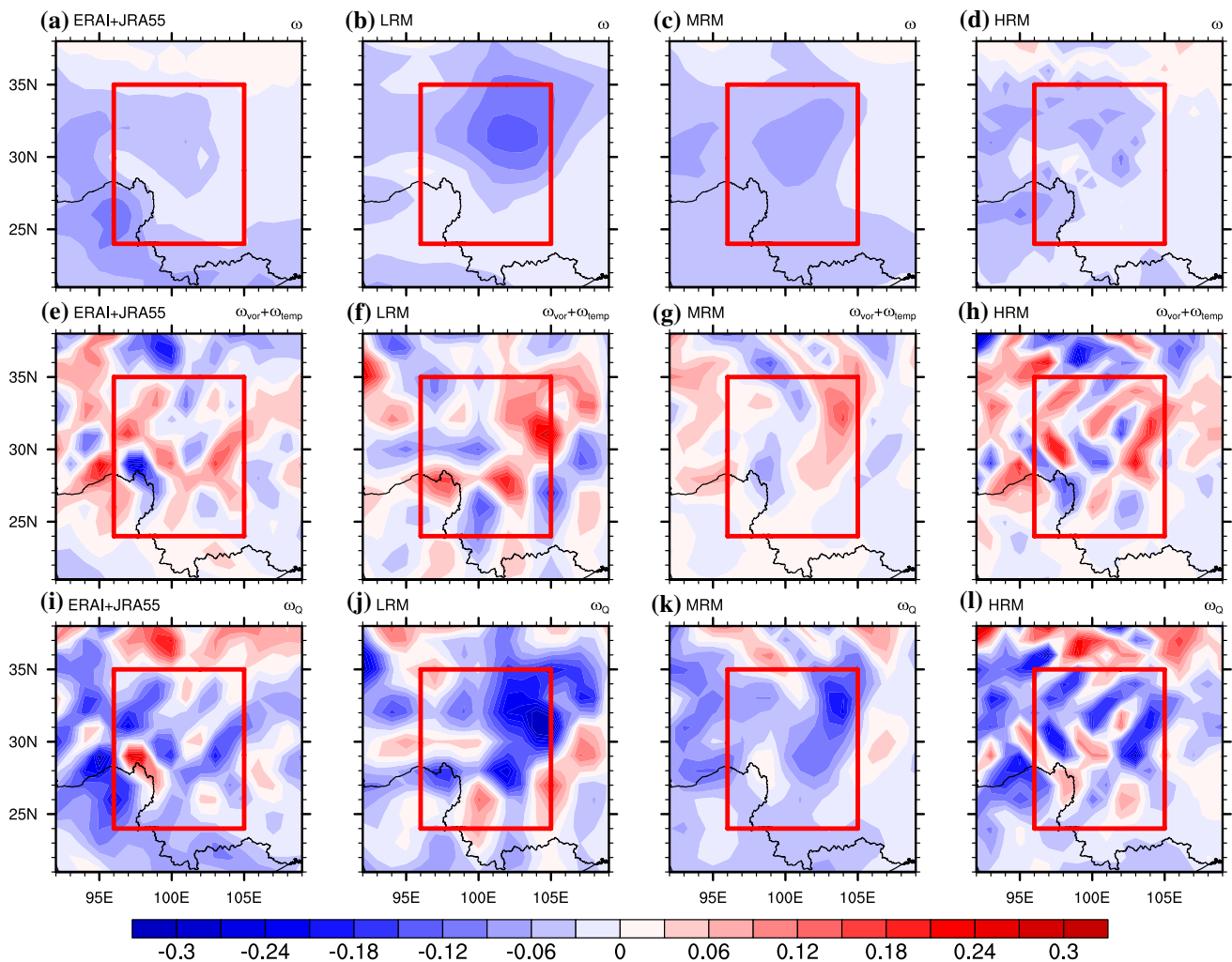


Fig. 9 Diagnosed climatological vertical velocity over HMs during rainy seasons in **a, e, i** reanalysis, **b, f, j** LRMs, **c, g, k** MRMs, and **d, h, l** HRMs. Shown from top to bottom panels are vertical velocity (ω ; Pa s^{-1}), the sum of vertical velocity due to the vertical difference of

vorticity horizontal advection and horizontal temperature advection ($\omega_{vor} + \omega_{temp}$; Pa s^{-1}), and vertical velocity due to diabatic heating (ω_Q ; Pa s^{-1})

centers in observation and reanalysis, but their location, range, and magnitude vary with models. As the horizontal resolution increases, the details of simulated precipitation pattern are improved and closer to observation and reanalysis, as well as the increasing magnitude of precipitation over the southwestern HMs. However, the simulated precipitation on the WSSB is overestimated regardless of resolution, probably due to the systematic biases of all AGCMs. Thus, the mechanisms involved in resolution affecting precipitation pattern and biases of precipitation on the WSSB are further examined.

According to the diagnosed results of moisture budget analysis, climatological rainy-season precipitation over HMs is mainly contributed by vertical moisture flux convergence. The simulated vertical moisture flux convergence is closer to reanalysis with the increase of model resolution, and observed details of vertical moisture flux convergence pattern are precisely captured in HRMs, especially over the southwestern HMs and on the WSSB. The vertical distribution of vertical moisture flux convergence in reanalysis and AGCMs highly resemble that of vertical velocity, emphasizing the crucial role of upward motions. The vertical moisture flux convergence is partially offset by horizontal moisture flux divergence, especially near the ridges of the Himalayas and HMs. In reanalysis, there is horizontal moisture flux convergence on windward slopes of the Himalayas, contributing to precipitation in the southwest corner of HMs. The details of horizontal moisture flux convergence are gradually captured with the increase of model resolution, resulting in that the precipitation over the southwestern HMs becomes stronger and its meridional range becomes wider.

Model resolution can influence simulations of both horizontal and vertical moisture flux convergence and further precipitation pattern over the southwestern HMs through resolution-related orographic effect, which includes the orographic barrier effect and orographically forced mechanical lifting. Compared with lower-resolution models, higher-resolution models can better resolve the complex topography, which weakens atmospheric circulation by increasing orographic roughness and further enhances the horizontal moisture flux convergence and upward motions. The observed magnitude, location, and range of horizontal moisture flux convergence and upward motions are also more effectively reproduced in higher-resolution models. Moreover, owing to orographically forced mechanical lifting, finer topography in higher-resolution models forces a more realistic magnitude and range of upward motions, as well as the vertical moisture flux convergence.

The vertical moisture flux convergence shows the dominant contribution to the precipitation on the WSSB and is related to the vertical distribution of upward motions. Thus, the biases of WSSB precipitation between reanalysis and AGCMs are attributed to the discrepancy in the

vertical distribution of upward motions. The resolution-related orographic barrier effect and orographically forced mechanical lifting play a similar role in the location and range of upward motions on the WSSB as over the southwestern HMs, and upward motions forced by orographic effect is close to surface. However, the simulated upward motions can reach a higher level than reanalysis, and a spurious center of upward motions develops at 400 hPa. By using omega equation analysis, it is found that the circulation-precipitation feedback is overestimated in AGCMs, leading to the upward motions at the higher levels and overestimation of WSSB precipitation.

This study reveals the importance of using HRMs to investigate the regional climate with complex topography, and also sheds light on the necessity of high-resolution reanalysis dataset that are assimilated by HRMs. An ongoing study evaluates the HMs precipitation in multiple high-resolution observational and reanalysis datasets, which include another two high-resolution reanalysis datasets—the National Centers for Environmental Prediction Climate Forecast System Reanalysis (CFSR; Saha et al. 2010; Saha et al. 2014) and the Modern-Era Retrospective Analysis for Research and Applications, Version 2 (MERRA2; Gelaro et al. 2017) besides ERAI and JRA55. The maximum precipitation center on the WSSB is overestimated in CFSR and MERRA2 and closer to observation in ERAI and JRA55 (Fig. S5). Preliminary analysis reveals that the excessive precipitation is probably related to the overestimation of circulation-precipitation feedback, indicating the consistent systematic biases in representation of moist convective processes in most models. In general, excessive circulation-precipitation feedback may originate from an internal bias of convective parameterization (Li and Xie 2012, 2014), which is always a key issue to improve models and deserves to further study.

Acknowledgements We acknowledge the World Climate Research Program's Working Group on Coupled Modeling, which is responsible for CMIP, and we thank the climate modeling groups (listed in Table 1 of this paper) for producing and making available their model output. For CMIP, the U.S. Department of Energy's Program for Climate Model Diagnosis and Intercomparison provides coordinating support and led development of software infrastructure in partnership with the Global Organization for Earth System Science Portals. We thank two anonymous reviewers as well as the editor for their useful comments. This work was supported by the Strategic Priority Research Program of Chinese Academy of Sciences (XDA20060501), the National Key R&D Program of China (2018YFA0605904), the National Natural Science Foundation of China (41705068, 41831175, 41425019, and 41721004), the China Postdoctoral Science Foundation (2016LH0005 and 2016M600116), the scholarship from China Scholarships Council under the State Scholarship Fund (201704910055), and the Natural Science Foundation of Guangdong Province (2016A030310009).

References

- Amante C, Eakins BW (2009) ETOPO1 1 Arc-Minute Global Relief Model: Procedures, Data Sources and Analysis. NOAA Technical Memorandum NESDIS NGDC-24, National Geophysical Data Center, NOAA, <https://doi.org/10.7289/v5d798bf>
- Ashfaq M, Rastogi D, Mei R, Touma D, Ruby Leung L (2017) Sources of errors in the simulation of south Asian summer monsoon in the CMIP5 GCMs. *Clim Dyn* 49:193–223. <https://doi.org/10.1007/s00382-016-3337-7>
- Barros AP, Lettenmaier DP (1993) Dynamic modeling of the spatial distribution of precipitation in remote mountainous areas. *Mon Weather Rev* 121:1195–1214. [https://doi.org/10.1175/1520-0493\(1993\)121%3c2254:MCCLIA%3e2.0.CO;2](https://doi.org/10.1175/1520-0493(1993)121%3c2254:MCCLIA%3e2.0.CO;2)
- Barros AP, Lettenmaier DP (1994) Dynamic modeling of orographically induced precipitation. *Rev Geophys* 32:265–284. <https://doi.org/10.1029/94rg00625>
- Cannon F, Carvalho LMV, Jones C, Norris J, Bookhagen B, Kiladis GN (2017) Effects of topographic smoothing on the simulation of winter precipitation in High Mountain Asia. *J Geophys Res Atmos* 122:1456–1474. <https://doi.org/10.1002/2016jd026038>
- Chen J, Bordoni S (2014) Orographic effects of the Tibetan plateau on the East Asian summer monsoon: an energetic perspective. *J Clim* 27:3052–3072. <https://doi.org/10.1175/jcli-d-13-00479.1>
- Chen C-S, Huang J-M (1999) A numerical study of precipitation characteristics over Taiwan Island during the winter season. *Meteorol Atmos Phys* 70:167–183. <https://doi.org/10.1007/s007030050032>
- Dai E, Wang Y, Ma L, Yin L, Wu Z (2018) 'Urban-Rural' gradient analysis of landscape changes around cities in mountainous regions: a case study of the Hengduan Mountain region in southwest China. *Sustainability* 10:1019
- Dee DP et al (2011) The ERA-Interim reanalysis: configuration and performance of the data assimilation system. *Q J R Meteorol Soc* 137:553–597. <https://doi.org/10.1002/qj.828>
- Dong W et al. (2016) Summer rainfall over the southwestern Tibetan Plateau controlled by deep convection over the Indian subcontinent. *Nat Commun* 7:10925. <https://doi.org/10.1038/ncomms10925>, <https://www.nature.com/articles/ncomms10925#supplementary-information>
- Dong D, Huang G, Tao W, Wu R, Hu K, Li C (2018) Interannual variation of precipitation over the Hengduan Mountains during rainy season. *Int J Climatol* 38:2112–2125. <https://doi.org/10.1002/joc.5321>
- Dong D, Tao W, Lau WKM, Li Z, Huang G, Wang P (2019) Interdecadal variation of precipitation over the Hengduan Mountains during rainy seasons. *J Clim* 32:3743–3760. <https://doi.org/10.1175/jcli-d-18-0670.1>
- Duan A, Hu J, Xiao Z (2013) The Tibetan Plateau summer monsoon in the CMIP5 simulations. *J Clim* 26:7747–7766. <https://doi.org/10.1175/jcli-d-12-00685.1>
- Fang S, Zhao Y, Han L, Ma C (2017) Analysis of landscape patterns of arid valleys in China, based on grain size effect. *Sustainability* 9:2263
- Ferretti R, Low-Nam S, Rotunno R (2000) Numerical simulations of the Piedmont flood of 4–6 November 1994. *Tellus A* 52:162–180. <https://doi.org/10.1034/j.1600-0870.2000.00992.x>
- Gelaro R et al (2017) The modern-era retrospective analysis for research and applications, Version 2 (MERRA-2). *J Clim* 30:5419–5454. <https://doi.org/10.1175/jcli-d-16-0758.1>
- Goswami BN (1998) Interannual variations of Indian summer monsoon in a GCM: external conditions versus internal feedbacks. *J Clim* 11:501–522. [https://doi.org/10.1175/1520-0442\(1998\)011%3c0501:ivoism%3e2.0.co;2](https://doi.org/10.1175/1520-0442(1998)011%3c0501:ivoism%3e2.0.co;2)
- Harada Y et al (2016) The JRA-55 reanalysis: representation of atmospheric circulation and climate variability. *J Meteorol Soc Jpn Ser II* 94:269–302. <https://doi.org/10.2151/jmsj.2016-015>
- Hertwig E, von Storch J-S, Handorf D, Dethloff K, Fast I, Krismer T (2015) Effect of horizontal resolution on ECHAM6-AMIP performance. *Clim Dyn* 45:185–211. <https://doi.org/10.1007/s00382-014-2396-x>
- Hu K, Xie S-P, Huang G (2017) Orographically anchored El Niño Effect on summer rainfall in central China. *J Clim* 30:10037–10045. <https://doi.org/10.1175/jcli-d-17-0312.1>
- Huang D-Q, Zhu J, Zhang Y-C, Huang A-N (2013) Uncertainties on the simulated summer precipitation over Eastern China from the CMIP5 models. *J Geophys Res Atmos* 118:9035–9047. <https://doi.org/10.1002/jgrd.50695>
- Huffman GJ et al (2007) The TRMM multisatellite precipitation analysis (TMPA): quasi-Global, multiyear, combined-sensor precipitation estimates at fine scales. *J Hydrometeorol* 8:38–55. <https://doi.org/10.1175/jhm560.1>
- Hughes M, Hall A, Fovell RG (2009) Blocking in areas of complex topography, and its influence on rainfall distribution. *J Atmos Sci* 66:508–518. <https://doi.org/10.1175/2008jas2689.1>
- Hunt KMR, Turner AG (2017) The effect of horizontal resolution on Indian monsoon depressions in the Met Office NWP model. *Q J R Meteorol Soc* 143:1756–1771. <https://doi.org/10.1002/qj.3030>
- Jiang Q (2003) Moist dynamics and orographic precipitation. *Tellus A: Dyn Meteorol Oceanogr* 55:301–316. <https://doi.org/10.3402/tellusa.v55i4.14577>
- Jin Q, Yang X-Q, Sun X-G, Fang J-B (2013) East Asian summer monsoon circulation structure controlled by feedback of condensational heating. *Clim Dyn* 41:1885–1897. <https://doi.org/10.1007/s00382-012-1620-9>
- Kang I-S et al (2002) Intercomparison of the climatological variations of Asian summer monsoon precipitation simulated by 10 GCMs. *Clim Dyn* 19:383–395. <https://doi.org/10.1007/s00382-002-0245-9>
- Katzfey JJ (1995) Simulation of extreme New Zealand precipitation events. Part I: sensitivity to orography and resolution. *Mon Weather Rev* 123:737–754. [https://doi.org/10.1175/1520-0493\(1995\)123%3c0737:soenzp%3e2.0.co;2](https://doi.org/10.1175/1520-0493(1995)123%3c0737:soenzp%3e2.0.co;2)
- Kitoh A, Kusunoki S (2008) East Asian summer monsoon simulation by a 20-km mesh AGCM. *Clim Dyn* 31:389–401. <https://doi.org/10.1007/s00382-007-0285-2>
- Kobayashi S et al (2015) The JRA-55 reanalysis: general specifications and basic characteristics. *J Meteorol Soc Jpn Ser II* 93:5–48. <https://doi.org/10.2151/jmsj.2015-001>
- Kripalani RH, Oh JH, Kulkarni A, Sabade SS, Chaudhari HS (2007) South Asian summer monsoon precipitation variability: coupled climate model simulations and projections under IPCC AR4. *Theor Appl Climatol* 90:133–159. <https://doi.org/10.1007/s00704-006-0282-0>
- Lau KM, Kim KM (2006) Observational relationships between aerosol and Asian monsoon rainfall, and circulation. *Geophys Res Lett*. <https://doi.org/10.1029/2006gl027546>
- Lau KM, Kim MK, Kim KM (2006) Asian summer monsoon anomalies induced by aerosol direct forcing: the role of the Tibetan Plateau. *Clim Dyn* 26:855–864. <https://doi.org/10.1007/s00382-006-0114-z>
- Li G, Xie S-P (2012) Origins of tropical-wide SST biases in CMIP multi-model ensembles. *Geophys Res Lett* 39:L22703. <https://doi.org/10.1029/2012gl053777>
- Li G, Xie S-P (2014) Tropical biases in CMIP5 multimodel ensemble: the excessive equatorial Pacific cold tongue and double ITCZ problems. *J Clim* 27:1765–1780. <https://doi.org/10.1175/jcli-d-13-00337.1>
- Li Z, He Y, Wang C, Wang X, Xin H, Zhang W, Cao W (2011) Spatial and temporal trends of temperature and precipitation during

- 1960–2008 at the Hengduan Mountains, China. *Quatern Int* 236:127–142. <https://doi.org/10.1016/j.quaint.2010.05.017>
- Li G, Xie SP, He C, Chen Z (2017) Western Pacific emergent constraint lowers projected increase in Indian summer monsoon rainfall. *Nat Clim Change* 7:708. <https://doi.org/10.1038/nclimate3387>, <https://www.nature.com/articles/nclimate3387#supplementary-information>
- López-Moreno JI, Goyette S, Beniston M (2008) Climate change prediction over complex areas: spatial variability of uncertainties and predictions over the Pyrenees from a set of regional climate models. *Int J Climatol* 28:1535–1550. <https://doi.org/10.1002/joc.1645>
- Maloney ED, Chelton DB (2006) An assessment of the sea surface temperature influence on surface wind stress in numerical weather prediction and climate models. *J Clim* 19:2743–2762. <https://doi.org/10.1175/jcli3728.1>
- Mishra SK, Anand A, Fasullo J, Bhagat S (2018) Importance of the resolution of surface topography in Indian monsoon simulation. *J Clim* 31:4879–4898. <https://doi.org/10.1175/jcli-d-17-0324.1>
- Ogata T, Johnson SJ, Schiemann R, Demory M-E, Mizuta R, Yoshida K, Arakawa O (2017) The resolution sensitivity of the Asian summer monsoon and its inter-model comparison between MRI-AGCM and MetUM. *Clim Dyn* 49:3345–3361. <https://doi.org/10.1007/s00382-016-3517-5>
- Prodhomme C, Batté L, Massonnet F, Davini P, Bellprat O, Guemas V, Doblas-Reyes FJ (2016) Benefits of increasing the model resolution for the seasonal forecast quality in EC-earth. *J Clim* 29:9141–9162. <https://doi.org/10.1175/jcli-d-16-0117.1>
- Roe GH (2005) Orographic precipitation. *Annu Rev Earth Planet Sci* 33:645–671. <https://doi.org/10.1146/annurev.earth.33.092203.122541>
- Saha S et al (2010) The NCEP climate forecast system reanalysis. *Bull Am Meteorol Soc* 91:1015–1058. <https://doi.org/10.1175/2010bams3001.1>
- Saha S et al (2014) The NCEP climate forecast system version 2. *J Clim* 27:2185–2208. <https://doi.org/10.1175/jcli-d-12-00823.1>
- Shang W, Ren X, Huang B, Cubasch U, Yang X-Q (2019) Subseasonal intensity variation of the South Asian high in relationship to diabatic heating: observation and CMIP5 models. *Clim Dyn* 52:2413–2430. <https://doi.org/10.1007/s00382-018-4266-4>
- Smith RB (1979) The influence of mountains on the atmosphere. *Adv Geophys B*. Saltzman, ed, Elsevier, 87–230
- Song Y, Qiao F, Song Z (2012) Improved simulation of the South Asian summer monsoon in a coupled GCM with a more realistic ocean mixed layer. *J Atmos Sci* 69:1681–1690. <https://doi.org/10.1175/jas-d-11-0235.1>
- Sperber KR, Hameed S, Potter GL, Boyle JS (1994) Simulation of the Northern Summer Monsoon in the ECMWF model: sensitivity to horizontal resolution. *Mon Weather Rev* 122:2461–2481. [https://doi.org/10.1175/1520-0493\(1994\)122%3c2461:soatns%3e2.0.co;2](https://doi.org/10.1175/1520-0493(1994)122%3c2461:soatns%3e2.0.co;2)
- Sperber KR et al (2013) The Asian summer monsoon: an intercomparison of CMIP5 vs. CMIP3 simulations of the late 20th century. *Clim Dyn* 41:2711–2744. <https://doi.org/10.1007/s00382-012-1607-6>
- Tao W, Huang G, Wu R, Hu K, Wang P, Chen D (2017) Asymmetry in summertime atmospheric circulation anomalies over the north-west Pacific during decaying phase of El Niño and La Niña. *Clim Dyn* 49:2007–2023. <https://doi.org/10.1007/s00382-016-3432-9>
- Tao W, Huang G, Wu R, Hu K, Wang P, Gong H (2018) Origins of biases in CMIP5 models simulating Northwest Pacific summertime atmospheric circulation anomalies during the decaying phase of ENSO. *J Clim* 31:5707–5729. <https://doi.org/10.1175/jcli-d-17-0289.1>
- Taylor KE, Stouffer RJ, Meehl GA (2011) An overview of CMIP5 and the experiment design. *Bull Amer Meteorol Soc* 93:485–498. <https://doi.org/10.1175/bams-d-11-00094.1>
- Ueda H, Ohba M, Xie S-P (2009) Important factors for the development of the Asian-Northwest Pacific summer monsoon. *J Clim* 22:649–669. <https://doi.org/10.1175/2008jcli2341.1>
- Wang L, Huang G, Chen W, Zhou W, Wang W (2018) Wet-to-dry shift over Southwest China in 1994 tied to the warming of tropical warm pool. *Clim Dyn* 51:3111–3123. <https://doi.org/10.1007/s00382-018-4068-8>
- Xu Y, Gao X, Shen Y, Xu C, Shi Y, Giorgi F (2009) A daily temperature dataset over China and its application in validating a RCM simulation. *Adv Atmos Sci* 26:763–772. <https://doi.org/10.1007/s00376-009-9029-z>
- Yao J, Zhou T, Guo Z, Chen X, Zou L, Sun Y (2017) Improved performance of high-resolution atmospheric models in simulating the East Asian summer monsoon rain belt. *J Clim* 30:8825–8840. <https://doi.org/10.1175/jcli-d-16-0372.1>
- You Q, Min J, Zhang W, Pepin N, Kang S (2015) Comparison of multiple datasets with gridded precipitation observations over the Tibetan Plateau. *Clim Dyn* 45:791–806. <https://doi.org/10.1007/s00382-014-2310-6>
- Zhang K, Pan S, Cao L, Wang Y, Zhao Y, Zhang W (2014) Spatial distribution and temporal trends in precipitation extremes over the Hengduan Mountains region, China, from 1961 to 2012. *Quat Int* 349:346–356. <https://doi.org/10.1016/j.quaint.2014.04.050>
- Zhou T, Li Z (2002) Simulation of the east asian summer monsoon using a variable resolution atmospheric GCM. *Clim Dyn* 19:167–180. <https://doi.org/10.1007/s00382-001-0214-8>

Publisher's Note Springer Nature remains neutral with regard to jurisdictional claims in published maps and institutional affiliations.